Compressed Sensing Electron Tomography of Needle-Shaped Biological Specimens - Potential for Improved Reconstruction Fidelity with Reduced Dose.

Zineb Saghi[(1)*], Giorgio Divitini[(1)], Benjamin Winter[(2)], Rowan Leary[(1)], Erdmann Spiecker[(2)], Caterina Ducati[(1)] and Paul A. Midgley[(1)*].

(1) Department of Materials Science and Metallurgy, University of Cambridge, 27 Charles Babbage Road, Cambridge, CB3 0FS, UK.

(2) Center for Nanoanalysis and Electron Microscopy (CENEM), Friedrich-Alexander-Universität Erlangen-Nürnberg, Cauerstraße 6, 91058 Erlangen, Germany.

Corresponding authors:

Zineb Saghi and Paul Midgley
Department of Materials Science and Metallurgy,
University of Cambridge,
27 Charles Babbage Road,
Cambridge, CB3 0FS.
Tel: +44 1223 334561
Emails: Z.S. (saghizineb@gmail.com) and P.A.M. (pam33@cam.ac.uk)

ABSTRACT

Electron tomography is an invaluable method for 3D cellular imaging. The technique is, however, limited by the specimen geometry, with a loss of resolution due to a restricted tilt range, an increase in specimen thickness with tilt, and a resultant need for subjective and time-consuming manual segmentation. Here we show that 3D reconstructions of needle-shaped biological samples exhibit isotropic resolution, facilitating improved automated segmentation and feature detection. By using scanning transmission electron tomography, with small probe convergence angles, high spatial resolution is maintained over large depths of field and across the tilt range. Moreover, the application of compressed sensing methods to the needle data demonstrates how high fidelity reconstructions may be achieved with far fewer images (and thus greatly reduced dose) than needed by conventional methods. These findings open the door to high fidelity electron tomography over critically relevant length-scales, filling an important gap between existing 3D cellular imaging techniques.

Keywords: electron tomography, isotropic resolution, compressed sensing, life science.

1. INTRODUCTION

A key challenge in life science microscopy is to image large cellular volumes while maintaining sufficient resolution to identify small features in their original cellular context [1,2]. Within the range of techniques employed for this purpose, electron tomography (ET) offers the highest 3D spatial resolution. Typically, samples are prepared as thin sections, and a series of bright field (BF) transmission electron microscope (TEM) images (projections) are acquired at successive tilt angles. The tilt series of images is then used as input for 3D reconstruction, often using a weighted backprojection (WBP) algorithm [3]. Whilst ET has enabled many new insights into the cellular world, two fundamental limitations still hamper attainment of highly accurate and reproducible results in an automated fashion.

The first limitation is related to the increase in effective sample thickness during tilt series acquisition: as the sample is tilted by angle θ, the projected thickness of a slab-like section increases by a factor of $1/\cos\theta$. This ultimately leads to a reduction in image contrast in BF-

TEM due to an increase in multiple scattering and inelastic scattering, the latter resulting in image blurring due to the chromatic aberration of the objective lens. Further, the limited depth of field (DOF) of the objective lens may lead to regions of the specimen being out of focus [4]. Reducing the angular increment between projections at high tilt angles, as in the Saxton scheme [5], or adjusting the exposure time so that all projections have similar SNR [6], are two acquisition strategies that may help improve the overall reconstruction quality, but the usable section thickness is still limited. Ellisman and co-workers explored the use of energy-filtered TEM to reduce chromatic blurring, imaging samples up to 3 μm thick and using an automated most-probable loss technique to choose the position of the energy selecting slit [4]. Alternatively, scanning TEM (STEM) offers advantages such as near-linearity of contrast and high signal-to-noise ratio (SNR), and the potential to reduce beam damage, as reported in [7-9]. Leapman and co-workers used BF-STEM to image 1 μm thick sections, achieving a resolution similar to that obtained by conventional BF-TEM for sections 300 nm thick [10,11]. Although chromatic aberration effects are negligible, STEM images are affected by beam divergence through the sample [10] and thus decreasing the incident convergence angle can lead to an increased DOF and improved 3D resolution. However, at high tilt angles, the thickness of the section may be larger than the DOF and ultimately beam broadening becomes the key factor limiting resolution.

Secondly, the geometry of conventional sample holders and the limited space within the pole piece gap of the TEM objective lens can restrict the tilt range to ca. ±70˚ or less. This leads to a 'missing wedge' of information in Fourier space, and corresponding artefacts in the reconstructions [12]. Segmentation of the reconstruction often needs to be performed in a manual fashion in order to extract features that may appear falsely elongated or faint. This can be laborious and more importantly subjective, leading to possible bias and non-repeatability.

Great effort has been expended in the biological and materials science communities to develop reconstruction methods that address the limited-angle tomography problem. Traditionally, using slab-like specimen geometries, the maximum required and maximum feasible number of projections is recorded following the so-called Crowther criterion for reconstruction resolution and the dose fractionation approach [3]. WBP reconstructions from datasets with a typical tilt range of ca. ±70˚ and an increment of 1˚-2˚ show good delineation of edges, but features with Fourier components in the missing wedge are highly corrupted and make automated segmentation difficult. Iterative reconstruction techniques such as simultaneous iterative

reconstruction technique (SIRT) [13] or algebraic reconstruction technique (ART) [14] can improve the reconstruction quality, but missing wedge artefacts are often still evident. Methods have been developed to address these limitations, including reconstruction algorithms such as discrete ART (DART) [15], regularization using total variation (TV) [16] and second partial derivatives [17], constrained maximum entropy [18] and equally-sloped tomography [19]; and post-processing routines ranging from anisotropic nonlinear diffusion [20] and bilateral denoising [21] to template matching tools [22]. Promising results have also been reported with more specific prior knowledge incorporated in such methods, as demonstrated in [23] with a shape-based reconstruction technique, and in [24] with a deformable template included in the template matching routine. However, a statistical evaluation performed in [24] showed that the amount of information extracted from the tomogram was still incomplete due to the missing wedge.

Another approach to the problem is to explore alternative acquisition strategies and specimen geometries. Dual-axis ET [25], wherein a second, mutually perpendicular tilt series is acquired, helps to minimize reconstruction artefacts by reducing the missing wedge to a 'missing pyramid'. However, it also implies additional electron dose (or, for a fixed total dose, lower dose per image), as well as challenges in aligning and merging the two tilt series to yield an optimum reconstruction [26]. The 'missing wedge' can be eliminated completely if the sample and holder are the correct geometry to enable a complete 180˚ rotation. Barnard et al. [27] fabricated a fully rotatable stage in which a glass micropipette, ca. 2 µm in diameter, was used as a sample support. However, the total sample thickness including the glass was sufficiently large that a 1 MeV microscope was needed to obtain suitable images. In a similar vein, Palmer et al. [28] used carbon nanopipettes (ca. 400 nm in diameter) attached to standard slot grids for cryo-ET at 300kV. Although this approach overcomes the increase of thickness at high tilt angles, as the pipettes were attached to a standard grid, the tilt range was limited to 145˚. Focused ion beam (FIB) (coupled with scanning electron microscopy, SEM) is used routinely in materials science for preparing needle-shaped specimens to enable so-called 'on-axis' ET using dedicated tomography holders (e.g. [29,30]). In the biological context, FIB has been employed mainly for 3D STEM viewing in the FIB-SEM (e.g. [31]) and for preparation of TEM lamellae [32] as an alternative to ultramicrotomy, avoiding artefacts such as diamond knife compression and non-flatness of the samples, especially under cryogenic conditions [33].

Here, we use the needle geometry for on-axis ET of a resin-embedded biological sample. We demonstrate that the method yields reconstructions with isotropic resolution and has the potential to bridge an important gap between ET of thin sections ca. 100 nm thick on the one hand, and FIB-SEM tomography [34] or serial sectioning of samples many microns in thickness [35] on the other. Moreover, the full tilt range dataset is used to show that, with compressed sensing (CS) reconstruction approaches, high fidelity reconstructions can be achieved with undersampled datasets, suggesting the possibility to reduce radiation dose.

2. METHODS

2.1 Section preparation

The sample analysed here comprises a stained resin-embedded portion of the nucleus accumbens shell from a rat brain. A male Sprague-Dawley rat (Harlan Laboratories Srl, S. Pietro al Natisone (UD)) was anesthetized with chloral hydrate (450 mg/kg) in accordance with the European and Italian legislation on the use and care of laboratory animals (EU Directive 2010/63 of September 22, 2010 and Italian D.L. 27.01 1992, n. 116). Under deep anesthesia, the rat was subjected to trans cardiac perfusion with ice-cold PBS (Phosphate Buffered Saline: 137 mM, 2.7 mM KCl, 10 mM Na_2HPO_4, 2 mM KH_2PO_4, pH 7.4), 2 % paraformaldehyde and 2 % glutaraldehyde. After perfusion, the brain was removed and post-fixed overnight in the same fixative used for transcardiac perfusion. Coronal brain sections (thickness: 40 μm) of the regions of interest, the nucleus accumbens, were cut according to the rat brain atlas of Paxinos and Watson [36] on ice-cold PBS with a vibratome (LeicaVT1000, Leica, Germany), kept in ice-cold PBS. For electron microscopy, the brain sections were post-fixed in 1 % osmium tetroxide in distilled water for 2 hours, stained overnight at 4 °C in an aqueous 0.5 % uranyl acetate solution, dehydrated in a graded ethanol series, infiltrated with propylene oxide and embedded in SPURR resin.

2.2 FIB-SEM needle-shaped sample preparation

The needle-shaped sample was prepared in a Helios Nanolab dual beam FIB-SEM (FEI company), equipped with a Ga^+ ion beam and a field emission gun SEM. The section was placed inside the FIB-SEM and a sequential set of images were analyzed using a slice-and-view approach until a region of interest was found.

A 4 µm thick platinum layer was deposited on the top surface in order to protect the selected region from implantation of Ga^+ ions (Figure S1(a)). The volume of interest was isolated by FIB milling over an annular area with an external diameter of 8 µm, leaving a central needle ~3 µm wide (Figure S1(b)). An additional rectangular trench was milled adjacent to the volume of interest, to allow the ion beam to reach the base of the needle and for it to be cut from the support. An Omniprobe micro-manipulator was then used to remove the needle, following a lift-out procedure [37], and weld it to a specimen cartridge compatible with the Fischione on-axis tomography holder (model 2050). Further annular thinning was carried out by employing lower currents, down to a value of 20 pA for a target diameter of ca. 450 nm. Figure S1(c) shows a low magnification view of the needle. Care was taken to ensure that the needle was parallel to the holder axis. This is crucial for eucentric specimen rotation, and for automated tracking and focusing. FIB-induced damage to the structural integrity of the sample was not observed, although a thin layer of Ga+ ions was detected by energy dispersive X-ray spectroscopy, in agreement with [33] (see Figure S2).

2.3 Tomography experiment

The boxed region in Figure S1(c) shows the region of the needle chosen for the ET experiment. An annular dark-field (ADF) STEM tilt series was acquired from -90˚ to +90˚ with 1˚ increment, using a TITAN³ 80-300 TEM (FEI company) equipped with a Schottky field-emission gun, a post-specimen Cs corrector (CEOS), a Fischione HAADF detector located above the viewing screen and a 2k x 2k Gatan CCD camera. Imaging conditions were as follows: accelerating voltage = 300 kV, extraction voltage = 4500V, gun lens = 6, microprobe mode, condenser aperture = 50 µm. A camera length of 145 mm (corresponding to a detector inner angle of 36 mrad) was used, seeking the best trade-off between SNR and mass-thickness contrast. The probe convergence semi-angle was 1.5 mrad, corresponding to a diffraction-limited probe size of ca. 0.8 nm and a DOF of ca. 650 nm, sufficient to encompass the needle diameter throughout the full tilt series. The effective spatial resolution in the ADF-STEM images depends on the probe diameter at the exit surface of the needle, and is estimated to be 4-5 nm for this experiment, taking into account the beam spreading from multiple elastic scattering [10]. The ADF-STEM tilt series was collected with Xplore3D software (FEI company), with each image comprising 2048x2048 pixels at 16-bit grayscale and with a pixel size of 0.8 nm. Automated tilting, tracking and focusing were performed before each image acquisition. Images were recorded with a frame time of 10 seconds, corresponding to a total acquisition time of 3 hours and electron dose of 3.4×10^6 e^-/nm^2. The stability of the needle

can be appreciated in the video of the tilt series (movie S5). Following acquisition, the tilt series was re-binned by a factor of 2 and aligned by cross-correlation using Inspect3D (FEI company). Weighted backprojection reconstructions were also performed using Inspect3D.
Although a needle provides a more restricted field of view in the *xy* plane (perpendicular to the electron beam) compared to conventional single-axis or dual-axis tomography using a slab-like section, a full tilt range with no missing wedge is accessible and the near-constant thickness profile of the needle sample enables acquisition of high quality data across the entire tilt series. There is no loss of resolution at high tilt angles or encroachment of features in part of the tilt series leading to truncated projection artefacts (the 'region-of-interest' problem) [38].

2.4 Compressed sensing electron tomography (CS-ET) reconstruction

To improve the reliability of the reconstructions from a limited number of projections, CS methods [39,40] are explored and compared to WBP. CS–ET has recently been applied successfully to inorganic materials [41-45], and was shown to be capable of generating high quality tomograms from a limited number of projections.

We give here only a brief description of the CS–ET algorithm. The foundation of CS theory and its application to ET can be found in [42] and references therein.

2.4.1 Principles of CS-ET

CS relies on two key principles: (1) sparsity (or compressibility) of the signal via an appropriate sparsifying transform, wherein the signal can be well-approximated in a more compact form (i.e. few coefficients with nonzero values); and (2) incoherence between the sampling and the sparsifying systems. In the context of CS-ET, acquiring projections around a tilt axis is, according to the Fourier slice theorem, equivalent to radial sampling in the Fourier domain. This form of sampling of Fourier space has been shown to be sufficiently incoherent to allow the application of CS to ET [39]. Appropriate choice of the sparsifying transform is signal/object-dependent, with the aim to capture the salient information content of the particular signal using a small number of coefficients. Common transforms are spatial finite-differences (leading to evaluation of the so-called 'total variation' (TV)) and wavelets, and simply the identity transform if the signal is intrinsically sparse in its native domain. TV-minimisation is often suitable for objects consisting of homogeneous regions with sharp edges, while piecewise smooth signals can be represented sparsely in a wavelet domain.

2.4.2 CS-ET applied to the needle-shaped sample

The CS-ET implementation used here was performed in MATLAB (MathWorks, Natick, MA) and is described in [42]. Reconstruction of the 3D tomogram was performed sequentially on independent 2D slices along the tilt axis. The images were first Fourier transformed to obtain radial samples of the object in the Fourier domain. An initial reconstruction was then obtained from the radial Fourier data using the non-uniform fast Fourier transform (*NUFFT*) developed by Fessler and Sutton [46]. In conjunction with the *NUFFT*, the conjugate gradient descent algorithm of Lustig *et al.* [39] was then used to solve the optimization problem defined by:

$$\hat{\mathbf{x}}_{\boldsymbol{\lambda}} = \arg\min_{\hat{\mathbf{x}}} \quad \{\|\Phi\hat{\mathbf{x}} - \mathbf{b}\|_{\ell_2}^2 \quad + \quad \lambda\|\Psi\hat{\mathbf{x}}\|_{\ell_1}\} \qquad \text{(eq. 1)}$$

where $\hat{\mathbf{x}}$ is the reconstruction of the true signal **x,** Φ is the undersampled Fourier transform operator, **b** is the Fourier transform of the acquired tilt series, and Ψ is the chosen sparsifying transform. The ℓ_1-norm term in (eq. 1) promotes sparsity in the chosen transform domain, and is defined as the sum of the absolute values. λ is a Lagrange multiplier that determines the relative importance of sparsity in the reconstruction. In essence, the algorithm promotes sparsity in the Ψ basis, subject to consistency with the measured data, which CS theory asserts is a powerful approach for recovering the signal.

For the needle-shaped specimen, sparsity was promoted in the image domain to retrieve the thin curve-like structures, and in the gradient domain for denoising purposes. In this case, (eq. 1) can be written as:

$$\hat{\mathbf{x}}_{\boldsymbol{\lambda_I, \lambda_{TV}}} = \arg\min_{\hat{\mathbf{x}}} \quad \{\|\Phi\hat{\mathbf{x}} - \mathbf{b}\|_{\ell_2}^2 \quad + \quad \lambda_I\|\Psi_I\hat{\mathbf{x}}\|_{\ell_1} \quad + \quad \lambda_{TV}TV(\hat{\mathbf{x}})\} \qquad \text{(eq. 2)}$$

where Ψ_I is the identity transform, and λ_I and λ_{TV} are weighting parameters that reflect the degree of sparsity imposed in the image and gradient domains, respectively. These λ_I and λ_{TV} values were chosen by visual assessment of reconstruction quality on selected slices, aiming for the optimal trade-off between minimization of reconstruction artefacts and loss of genuine signal. In particular, λ_{TV} was carefully chosen: setting λ_{TV} too high would reduce the noise and streaking artefacts, but also lead to erroneous flattening of the edges (i.e. loss of high frequency details) and merging of closely spaced features.

2.5 Visualisation and post-processing

Voxel projection views were generated in Avizo Fire (Visualization Sciences Group), while orthoslices through the tomographic reconstruction were produced in ImageJ [47].

Resolution estimation was performed by calculating a Fourier Shell Correlation (FSC) curve in Bsoft [48]. Tomograms were calculated from even and odd members of the -90˚:1˚:+90˚ tilt series. A mask was then applied to the tomograms to restrict the FSC to the needle region, thus reducing the influence of the background (i.e. vacuum). The resolution estimate was determined at a threshold of 0.3. The algorithm implemented in Bsoft is described in details in [49].

The quality of the reconstructions was also assessed by calculating the peak signal-to-noise ratio (PSNR). This was estimated using the SNR plugin provided by the Biomedical Image Group, EPFL, Switzerland (http://bigwww.epfl.ch/sage/soft/snr/). The definition of PSNR is given in (eq. 3), where *r* is the reference image and *t* is the test image. For the analysis here, *r* is the reconstruction from a fully sampled dataset and *t* is the reconstruction obtained from datasets with angular undersampling. The higher the PSNR, the higher the fidelity of the reconstruction. A perfect recovery would lead to a PSNR value of infinity.

$$\mathrm{PSNR} = \ 10.\log_{10}\left[\frac{\max\left(r(x,y)\right)^2}{\frac{1}{n_x.n_y}.\sum_0^{n_x-1}\sum_0^{n_y-1}[r(x,y)-t(x,y)]^2}\right] \qquad \text{(eq. 3)}$$

3. RESULTS

3.1 Isotropic ET reconstructions

Figure 1(a) displays a voxel projection of a WBP reconstruction, where high fidelity 3D structural information is evident, uncorrupted by missing wedge or truncation artefacts. This can be appreciated in the *yz* and *xy* orthoslices (b and c) highlighting the presence of synaptic vesicles with a uniform shape and mitochondria with resolved double membranes (inset in (c)). Cross-sectional slices (d) through an excitatory synapse and (e) a mitochondrion further illustrate the isotropic retrieval of features with the absence of missing wedge artefacts (slices through the entire 3D reconstruction of the needle, in *xy* and *xz* planes, are shown in the movie S6).

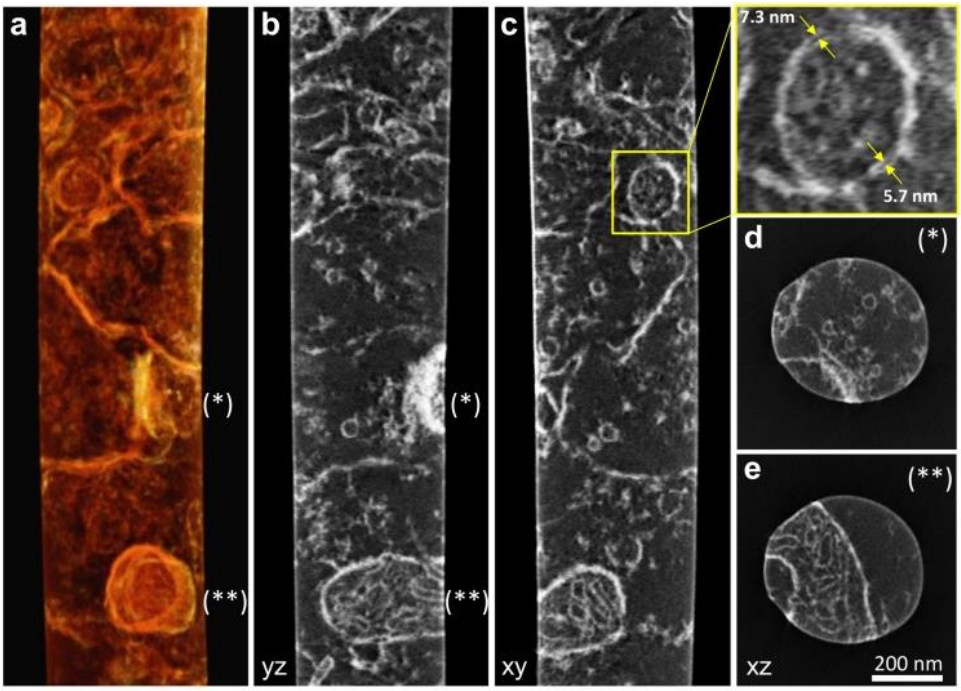

Figure 1 ADF-STEM tomography of a needle-shaped sample, from a portion of the nucleus accumbens shell of a rat brain. (a) Voxel projection rendering of the 3D reconstruction from an ADF-STEM tilt series (-90˚:1˚:+90˚), showing an excitatory synapse (*) and a mitochondrion (**). (b) *yz*, (c) *xy* and (d,e) *xz* slices through the needle (where the *z* direction is parallel to the electron beam at 0˚ sample tilt) highlight some of the features indicated in (a). The yellow inset in (c) show resolved lipid bilayers. Isotropic 3D resolution is achieved, as confirmed by the uniform shape of the synaptic vesicles in all three orthogonal directions (b-d).

In addition, segmentation can be performed more readily and robustly than on reconstructions from limited angle datasets. To illustrate this, Figure 2 shows results of automated thresholding using the Bernsen method [50] to segment the synaptic vesicle shown in Figure 2(a). When projections spanning the full tilt range are available, the vesicle is reliably segmented with uniform visibility of the membranes. If, however, the tilt range is artifically reduced to mimic the restricted tilt range of a conventional slab-like section, the missing wedge of information induces blurring and elongation. Automated segmentation routines then fail to retrieve membranes whose normals lie in the missing wedge. The continuity of the vesicle is then lost, and manual segmentation with prior knowledge about the expected shape would be necessary to attempt to label such features – a challenging and subjective task.

Missing wedge artefacts are especially pronounced when seeking to image objects that have elongated features perpendicular to the optic axis. In this case, the features are partially or completely lost due to important Fourier components lying in the missing wedge. This can be appreciated in Figure 2 by noting how the horizontal portion of the postsynaptic membrane (indicated in red inset) becomes faint as the tilt range is reduced. Similar critical loss of information has been demonstrated previously, e.g. concerning CdTe tetrapods [51], block copolymers with cylindrical microdomains [52], and actin filament networks [24]. Dual-axis tomography partially, but not entirely, reduces these artefacts [26,51,52]. Full tilt range on-axis tomography of such structures within a needle-shaped specimen, however, completely eliminates them.

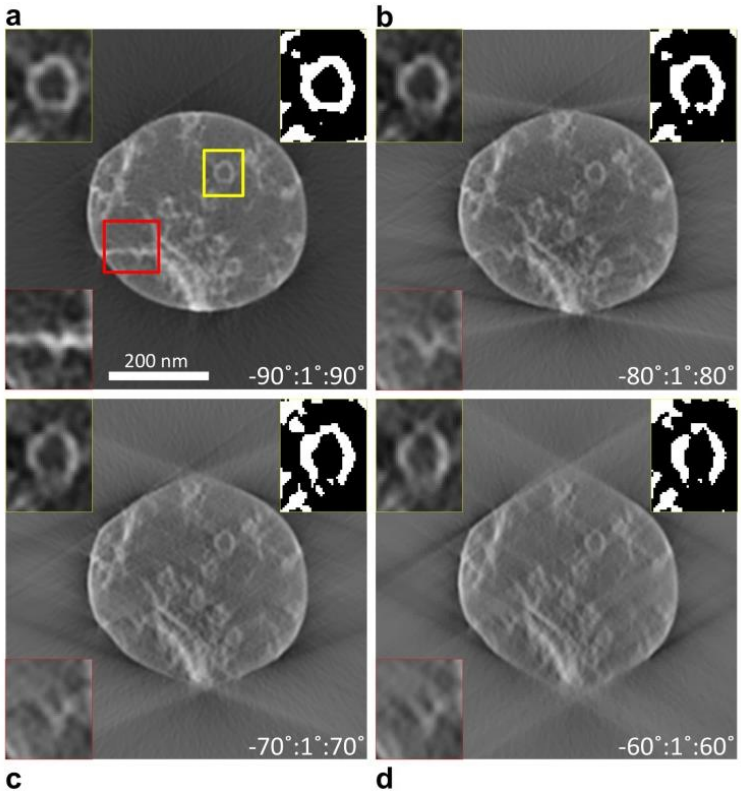

Figure 2 Cross-sectional slices through the reconstructed synapse region obtained from a tilt series with 1˚ increment and deliberately introduced restricted tilt ranges. (a) Isotropic resolution is achieved with full tilt range on-axis ET. (b-d) Artefacts such as elongation and blurring of a synaptic vesicle (yellow insets) and the reduced contrast of a region of the postsynaptic membrane (red insets) are observed on reconstructions obtained from limited angular ranges of 160˚, 140˚ and 120˚, respectively. Local thresholding by Bernsen method (top right insets) successfully segments the full tilt range reconstruction (a),

but fails to retrieve the complete synaptic vesicle in the case of limited angle tomography (b-d).

To further illustrate the improvements, a region of the needle containing the mitochondrion, with both vertical and horizontal cristae, was selected for additional analysis. Figure 3 shows a cross-sectional slice from a reconstruction with no missing wedge, and reconstructions using a restricted angular range of ±60˚. The anisotropic degradation caused by a limited tilt range is shown by simulating two different missing wedge directions (see Figure S3). Horizontal membranes are absent when the missing wedge direction is vertical (Figure 3(b)), vertical membranes are absent when it is horizontal (Figure 3(c)), while the reconstruction from the full tilt series (no missing wedge) retrieves all features (Figure 3(a)). Moreover, closely spaced features that are clearly separated in a full tilt range reconstruction are erroneously merged in the limited angle reconstructions; see for example the falsely merged features indicated by the vertical arrows in the insets of the top images in Figures 3(b,c).

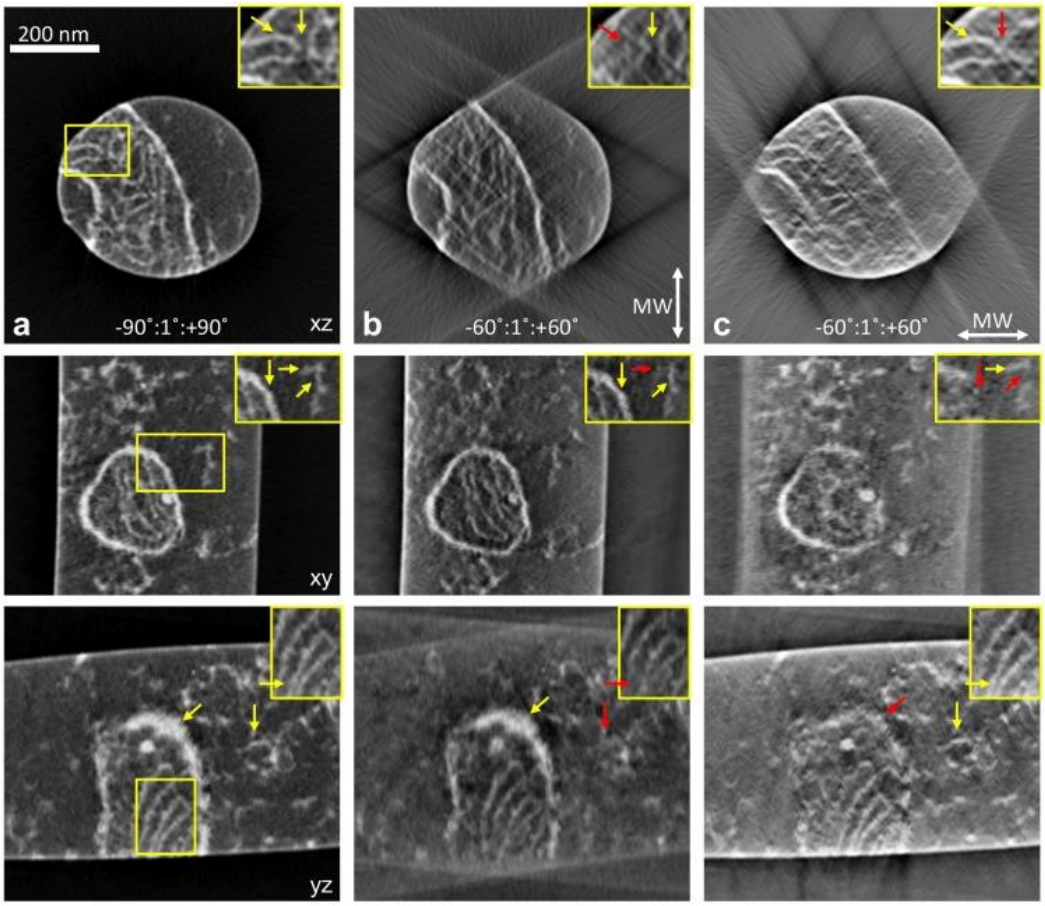

Figure 3 The anisotropic effect of the missing wedge direction on feature visibility. Yellow arrows indicate key linear features that are retrieved, while red ones indicate those

that are not successfully reconstructed according to the orientation of the missing wedge. (a) Isotropic recovery of all lines from the full tilt range acquisition. (b) Orthoslices through the reconstructed mitochondrion where only a ±60˚ portion of the full tilt series has been used, and with the missing wedge (MW) in the *z* direction. Features lying preferentially in the *x* direction are faint or absent. (c) Orthoslices of a reconstruction with the same tilt range as (b), but the missing wedge of the tilt series lying in the *x* direction. Features lying preferentially in the *z* direction are faint or absent. Additionally, the inset in (c) (top row) highlights features being falsely merged by the blurring induced by the missing wedge.

3.2 CS-ET for 3D cellular imaging

In this work, we took advantage of the availability of a full tilt range experimental dataset to explore compressed sensing (CS) reconstruction approaches, with the aim to improve the fidelity of the reconstructions and reduce the total dose without loss of structural information. WBP reconstructions from datasets with a full tilt range but a large tilt increment suffer from severe artefacts and low SNR. Figure 4 shows orthoslices through the mitochondrion, obtained from a full-range tilt series and with different degrees of undersampling. Streaking artefacts (also called 'fanning' artefacts) are visible in tomograms obtained with 45 (figure 4(c)) and 26 projections (Figure 4(d)), and make the segmentation challenging. Reconstructions from 180 or 90 projections (corresponding to 1˚ and 2˚ increments, respectively) are visually very similar (Figure 4(a) and (b), respectively), suggesting that a 2˚ increment is sufficient when the full tilt range is available. This can be appreciated in the automated segmentation of the selected box in Figure 4(a): the continuity of the membranes is well preserved when datasets with 1˚ and 2˚ increments are available, but lost for higher undersampling.

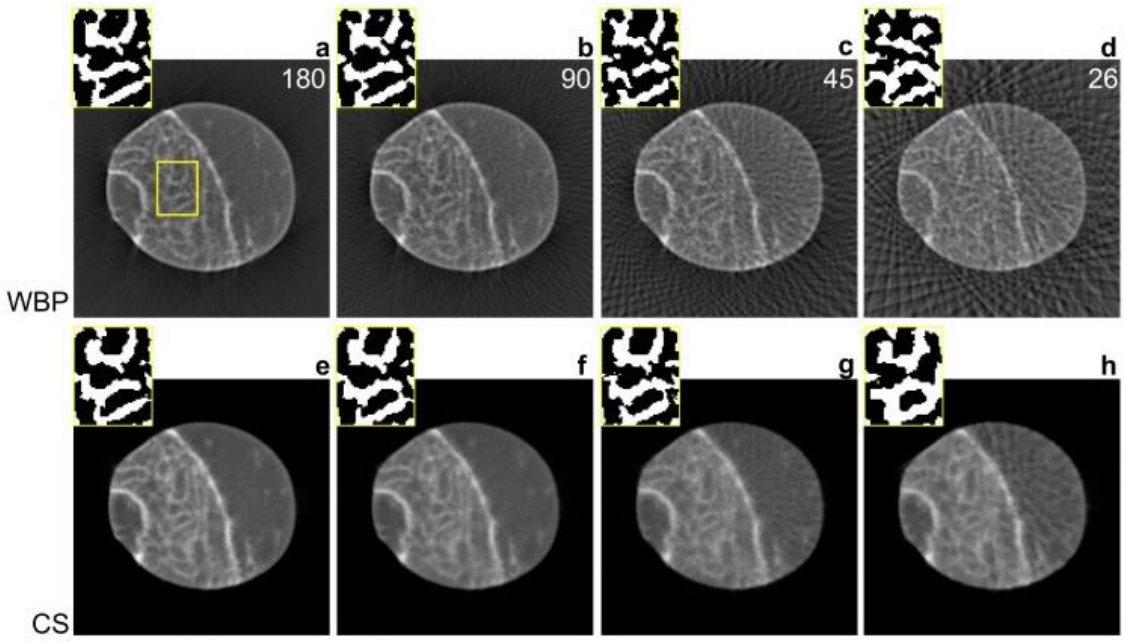

Figure 4 Orthoslices through the mitochondrion, reconstructed from a full tilt range acquisition with different degrees of undersampling. The number of projections used is shown on the images. Top row images (a-d) are WBP reconstructions while the bottom row (e-h) show those obtained with CS-ET. For a qualitative comparison of WBP and CS-ET, automated local thresholding by the Bernsen method was applied to the boxed region in (a) (insets). For highly undersampled datasets, the continuity of the membranes is better preserved in the CS-ET reconstructions.

As shown in Figure 4(a,b) and (e,f), for highly sampled datasets, CS-ET appears to perform similarly to WBP. However, as the number of projections is reduced, the inner membranes in the CS-ET reconstructions remain visible and are less affected by streaking artefacts compared to the WBP reconstructions. Moreover, automated segmentation of CS-ET data yielded much improved results compared to WBP on the reconstructions from 26 or 45 projections (see insets in Figure 4(c,d) and (g,h)).

The fidelity of the CS-ET reconstructions can be quantified using the peak-signal-to-noise-ratio (PSNR), with the fully sampled reconstruction as a reference (Figure 5) [53]. Although this is only one of many possible measures of the reconstruction fidelity, it suffices to reinforce the trends clearly visible in Figure 4: for highly sampled datasets, WBP and CS-ET have a similar PSNR, but as the number of projections is reduced, CS-ET consistently achieves visually interpretable reconstructions with high PSNR values. This is key to permitting reliable segmentation, even when just 26 projections are used for reconstruction.

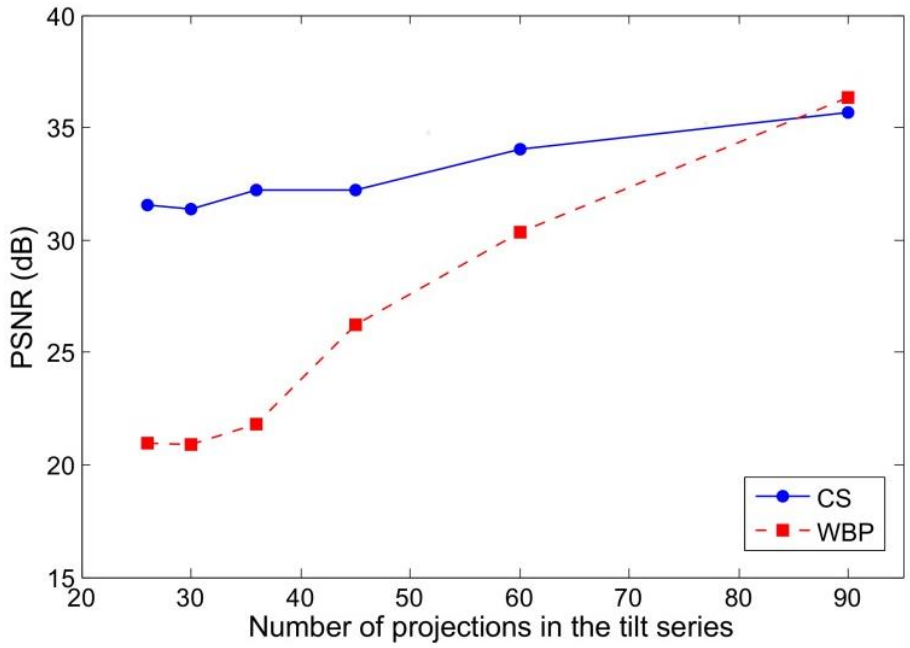

Figure 5 PSNR for WBP and CS-ET reconstructions as a function of the number of projections spanning the full 180˚ tilt range. The fully sampled (1˚ increment) reconstructions were used as references.

A reduced number of projections, and therefore total dose, implies that using CS-ET type reconstruction algorithms it is now possible to characterize samples that have previously been considered too beam sensitive for ET. Interestingly also, spreading the dose over fewer projections may lead to higher fidelity reconstructions using regularization techniques. More generally, in the context of further reconstruction algorithm development, the full tilt range datasets possible using a needle sample can be used to empirically evaluate advanced reconstruction algorithms and the limits in which further post-processing can be robustly applied, such as automated labelling and template matching methods.

4. DISCUSSION

Accurate 3D cellular density maps obtained by ET are critical for successful docking of macromolecular structures derived from higher resolution imaging techniques, such as single particle analysis, X-ray crystallography or nuclear magnetic resonance [54]. The needle-like geometry offers a way to generate faithful cellular landscapes with isotropic resolution. The constant thickness throughout the tilt series implies that fields of view of a few microns are accessible, potentially including whole cells and organelles. A resolution of 6.3 nm was

estimated by Fourier shell correlation (Figure S4), which could be improved by exploring other imaging conditions for the same sample thickness [10]. Ultimately, there is almost always a compromise between field of view and resolution, according to the Crowther criterion [3]. ET of needle-shaped specimen may be considered as a complementary technique to FIB-SEM tomography, which can image larger volumes but whose spatial resolution is highly anisotropic. Each slice imaged in the FIB-SEM process has a lateral resolution governed by the SEM optics and sample interaction; typically 3-4 nm [34], with the possibility to reach 1 nm [32]. However, slice thicknesses of (at best) 5-10 nm lead to a depth resolution of 10-20 nm (according to Nyquist criterion).

Identifying a region of interest for ET is a challenge in biology and usually involves correlative light and electron microscopy, and the screening of many slab-like sections [55]. A similar challenge is faced when preparing needle samples. One approach to identify a buried region of interest would be to follow the *correlative TEM and FIB-SEM* approach suggested by Hernandez-Saz et al. [56]: a thick section can be prepared by FIB-SEM and marked with features that are visible both in TEM and SEM. The region of interest is then identified by TEM and a needle is subsequently milled by FIB-SEM.

As seen in movie S5, and after comparison of the first and last image acquired in the tilt series, little shrinkage (< 2 %) and beam damage was observed, even though the dose was not optimized in this particular experiment. This may be attributed to the conductive Ga^+ layer acting as a protective and stabilizing shell, and suggests that higher doses could be employed on FIB-prepared samples, both at room temperature and in cryogenic conditions [33, 57]. The advantages of a similar metallic layer in close proximity to a biological specimen were reported recently by Russo et al. [58] using gold support films for cryo-microscopy.

Finally, while WBP is the most widely used algorithm in biological ET, we show that CS is capable of producing high fidelity reconstructions even when applied to datasets with significant angular undersampling (i.e. large tilt increment). Further undersampling may be achievable by spatial low-dose acquisition strategies using the scanning mode. Since CS-ET resolution is dependent on fine scale sampling of the projections [59], one approach to speed up the acquisition is to scan the beam to acquire data at only selected (e.g. randomly chosen) pixel positions while keeping a large frame size (say 2048x2048), and use inpainting algorithms to retrieve the full frame [53, 60]. In particular, as recently shown by some of the authors [60], a dose reduction of 10x is possible when pixel subsampling is combined with

angular subsampling and CS reconstruction. We believe this undersampling approach will prove to be advantageous for ET experiments in both life sciences and materials science. In general, using CS approaches and prior knowledge, acquiring relatively few data points (pixels in each image and/or number of projections in a tilt series) but each with relatively high SNR may lead to an improved reconstruction compared to the conventional dose fractionation approach. Most interestingly, templates of macromolecular structures could be used as prior knowledge, effectively performing the reconstruction and docking simultaneously, compared to the classical post-processing steps of denoising followed by template matching.

5. CONCLUSIONS

In summary, we have shown how needle-shaped specimens offer a new approach for ET of biological structures without missing wedge artefacts. High fidelity 3D reconstructions with an order of magnitude reduction in dose are now achievable using a needle sample geometry combined with CS reconstruction.

ACKNOWLEDGEMENTS

R. Marotta is gratefully acknowledged for providing the biological sample and giving constructive comments on the manuscript. We thank J.J. Fernandez for his assistance in the resolution estimation by FSC, and B. Butz for his help with the TEM measurements. The research leading to these results has received funding from the European Union Seventh Framework Programme under Grant Agreement 312483 - ESTEEM2 (Integrated Infrastructure Initiative–I3), as well as from the European Research Council under the European Union's Seventh Framework Programme (FP/2007-2013)/ERC grant agreement 291522 - 3DIMAGE. B.W. and E.S. acknowledge financial support from the Deutsche Forschungsgemeinschaft (DFG) within the framework of the SPP 1570 as well as through the Cluster of Excellence "Engineering of Advanced Materials" at the Friedrich-Alexander-Universität Erlangen-Nürnberg. G.D. and C.D. acknowledge funding from the ERC under grant number 259619 PHOTO EM. B.W. acknowledges the Research Training Group "Disperse Systems for Electronic Applications" (DFG GEPRIS GRK 1161). R.L. acknowledges a Junior Research Fellowship from Clare College. All data accompanying this publication are directly available within the publication.

REFERENCES

[1] Stahlberg, H, Watz, T (2008) Molecular electron microscopy: state of the art and current challenges. *ACS Chem Biol* 5:268-281.

[2] Lucic, V, Forster, F, Baumeister, W (2005) Structural studies by electron tomography: from cells to molecules. *Annu Rev Biochem* 74:833-865.

[3] Frank, J (2006) *Electron Tomography: Methods for Three-Dimensional Visualization of Structures in the Cell* (Springer).

[4] Bouwer, JC et al. (2004) Automated most-probable loss tomography of thick selectively stained biological specimens with quantitative measurement of resolution improvement. *J Struct Biol* 148:297-306.

[5] Saxton, WO, Baumeister, W, Hahn, M (1984) The three-dimensional reconstruction of imperfect two-dimensional crystals. *Ultramicroscopy* 13:57–70.

[6] Grimm, R et al. (1998) Electron tomography of ice-embedded prokaryotic cells. *Biophys J* 74:1031-1042.

[7] Kazuhiro, A, Takagi, T, Hirase, A, Miyazawa, A (2008) STEM tomography of thick biological specimens. *Ultramicroscopy* 109:70-80.

[8] Buban, JP, Ramasse, Q, Gipson, B, Browning, ND, Stahlberg, H (2010) High-resolution low-dose scanning transmission electron microscopy. *J Electron Microsc* 59:103–112.

[9] Wolf, SG, Houben, L, Elbaum, M (2014) Cryo-scanning transmission electron tomography of vitrified cells. *Nat Methods* 11:432-428.

[10] Hohmann-Marriott, MF et al. (2009) Nanoscale 3D cellular imaging by axial scanning transmission electron tomography. *Nat Methods* 6:729–731.

[11] Sousa, AA, Azari, AA, Zhang, GF, Leapman, RD (2011) Dual-axis electron electron tomography of biological specimens: extending the limits of specimen thickness with bright-field STEM imaging. *J Struct Biol* 174:107–114.

[12] Fernandez, JJ (2012) Computational methods for electron tomography. *Micron* 43:1010-1030.

[13] Gilbert, P (1972) Iterative methods for the three-dimensional reconstruction of an object from projections. *J Theor Biol* 36:105-117.

[14] Gordon, R, Bender, R, Herman, GT (1970) Algebraic reconstruction techniques (Art) for 3-dimensional electron microscopy and X-ray photography. *J Theor Biol* 29:471–476.

[15] Batenburg, KJ et al. (2009) 3D imaging of nanomaterials by discrete tomography. *Ultramicroscopy* 109:730-740.

[16] Aganj, I et al. (2007) Regularization for inverting the Radon transform with wedge consideration. *Proc 4th IEEE Int Symp Biomedical Imaging: From Nano to Macro (ISBI2007)* 217-220.

[17] Do, S, Karl, WC, Kalra, MK, Brady, TJ, Pien, H (2010) A variational approach for reconstructing low dose images in clinical helical CT. *Proc. 2010 IEEE Int. Symp. Biomedical Imaging: From Nano to Macro (ISBI2010)* 784-787.

[18] Skoglund, U, Ofverstedt, LG, Burnett, RM, Bricogne, G (1996) Maximum-entropy three-dimensional reconstruction with deconvolution of the contrast transfer function: a test application with adenovirus. *J Struct Biol* 117:173–188.

[19] Lee, E et al. (2008) Radiation dose reduction and image enhancement in biological imaging through equally-sloped tomography. *J Struct Biol* 164:221–227.

[20] Frangakis, AS, Hegerl, R (2001) Noise reduction in electron tomographic reconstructions using nonlinear anisotropic diffusion. *J Struct Biol* 135:239–250.

[21] Jiang, W, Baker, ML, Wu, Q, Bajaj, C, Chiu, W (2003) Applications of a bilateral denoising filter in biological electron microscopy. *J Struct Biol* 144:114-122.

[22] Lebbink, MN et al. (2007) Template matching as a tool for annotation of tomograms of stained biological structures. *J Struct Biol* 158:327-335.

[23] Gopinath, A et al. (2012) Shape-based regularization of electron tomographic reconstruction. *IEEE Trans Med Imag* 31:2241-2252.

[24] Rigort, A et al. (2012) Automated segmentation of electron tomograms for a quantitative description of actin filament networks. *J Struct Biol* 177:135-144.

[25] Mastronarde, DN (1997) Dual-axis tomography: an approach with alignment methods that preserve resolution. *J Struct Biol* 120:343–352.

[26] Tong, J, Arslan, I, Midgley, PA (2006) A novel dual-axis iterative algorithm for electron tomography. *J Struct Biol* 153:55-63.

[27] Barnard, DP, Turner, JN, Frank, J, McEwen, BF (1992) A 360º single-axis stage for the high-voltage electron microscope. *J Microsc* 167:39-48.

[28] Palmer, CM, Lowe, J (2014) A cylindrical specimen holder for electron cryo-tomography. *Ultramicroscopy* 137(100):20-29.

[29] Kawase, N, Kato, M, Nishioka, H, Jinnai, H (2007) Transmission electron microtomography without the "missing wedge" for quantitative structural analysis. *Ultramicroscopy* 107:8-15.

[30] Divitini, G et al. (2014) Nanoscale analysis of a hierarchical hybrid solar cell in 3D. *Adv Func Mater* 24:3043-3050.

[31] Kamino, T, Yaguchi, T, Ohnishi, T, Ishitani, T, Osumi, M (2004) Application of a FIB-STEM system for 3D observation of a resin-embedded yeast cell. *J Elect Microsc* 53:563-566.

[32] Heymann, JAW et al (2006) Site-specific 3D imaging of cells and tissues with a dual beam microscope. *J Struct Biol* 155:63-73.

[33] Marko, M, Hsieh, C, Schalek, R, Frank, J, Mannella, C (2007) Focused-ion-beam thinning of frozen-hydrated biological specimens for cryo-electron microscopy. *Nat Methods* 4:215-217.

[34] Knott, G, Marchman, H, Wall, D, Lich, B (2008) Serial section scanning electron microscopy of adult brain tissue using focused ion beam milling. *J Neurosc* 28:2959-2964.

[35] Hanssen, E et al (2010) Whole cell imaging reveals novel modular features of the exomembrane system of the malaria parasite, *Plasmodium falciparum*. *Int J Parasit* 40:123-134.

[36] Paxinos, G, Watson, C (1998) *The Rat Brain in Stereotaxic Coordinates*. 4th Edn San Diego, CA (Academic Press).

[37] Giannuzzi, LA, Stevie, FA (2005). *Introduction to Focused Ion Beams* (Springer, New York).

[38] Natterer, F (2001) *The Mathematics of Computerized Tomography. Classics in Applied Mathematics* (Society for Industrial and Applied Mathematics, Philadelphia).

[39] Lustig, M, Donoho, D, Pauly, JM (2007) Sparse MRI: The application of compressed sensing for rapid MR imaging. *Magn Reson Med* 58:1182-1195.

[40] Candès, EJ, Wakin, MB (2008) An introduction to compressive sampling. *IEEE Signal Proc Mag* 25:21-30.

[41] Saghi, Z et al (2011) 3D Morphology of iron oxide nanoparticles with reactive concave surfaces – a compressed sensing-electron tomography (CS-ET) appproach. *Nano Letters* 11: 4666-4673.

[42] Leary, R, Saghi, Z, Midgley, P, Holland, DJ (2013) Compressed sensing electron tomography. *Ultramicroscopy* 131:70–91.

[43] Nicoletti, O et al. (2013) Three-dimensional imaging of localized surface plasmon resonances of metal nanoparticles. *Nature* 502:80-84.

[44] Leary, R, Midgley, P, Thomas, JM (2012) Recent advances in the application of electron tomography to materials chemistry. *Acc Chem Res* 45:1782-1791.

[45] Goris, B et al (2012) Atomic-scale determination of surface facets in gold nanorods. *Nat Mater* 11:930-935.

[46] Fessler, JA, Sutton, BP (2003) Non uniform fast Fourier transforms using min-max interpolation. *IEEE Trans Sig Proc* 51:560-574.

[47] Schneider, CA, Rasband, WS, Eliceiri, KW (2012) NIH Image to ImageJ: 25 years of image analysis. *Nat Methods* 9:671-675.

[48] Heymann, JB (2001) Bsoft: Image and molecular processing in electron microscopy. *J Struct Biol* 133:156-169.

[49] Cardone, G, Grunewald, K, Steven, AC (2005) A resolution criterion for electron tomography based on cross-validation. *J Struct Biol* 151(2):117-129.

[50] Bernsen, J (1986) Dynamic thresholding of grey-level images. *Proc of the 8th Int Conf Patt Recog*.

[51] Arslan, I, Tong, JR, Midgley, P (2006) Reducing the missing wedge: high-resolution dual axis tomography of inorganic materials. *Ultramicroscopy* 106:994-1000.

[52] Sugimori, H, Nishi, T, Jinnai, H (2005) Dual-axis electron tomography for three-dimensional observation of polymeric nanostructures. *Macromolecules* 38:10226-10233.

[53] Stevens, A, Yang, H, Carin, L, Arslan, I, Browning, ND (2014) The potential for Bayesian compressed sensing to significantly reduce electron dose in high-resolution STEM images. *Microscopy* 63:41-51

[54] Carol V, Robinson, CV, Sali, A, Baumeister, W (2007) The molecular sociology of the cell. *Nature* 450:973-982.

[55] Plitzki, JM, Rigort, A, Leis, A (2009) Correlative cryo-light microscopy and cryo-electron tomography: from cellular territories to molecular landscapes. *Curr Opinion in Biotechn.* 20(1):83-89.

[56] Hernandez-Saz, J, Herrera, M, Molina, SI (2012) A methodology for the fabrication by FIB of needle-shape specimens around sub-surface features at the nanometer scale. *Micron* 43: 643-650.

[57] Rigort, A et al (2012) Focused ion beam micromachining of eukaryotic cells for cryoelectron tomography. *Proc Natl Acad Sci USA* 109(12):4449-4454.

[58] Russo, CJ, Passmore, LA (2014) Ultrastable gold subtrates for electron cryomicroscopy. *Science* 346:1377-1380.

[59] Roman, B, Adcock, B, Hansen, A (2014) On asymptotic structure in compressed sensing. *arXiv:1406.4178v2 [math.FA]*.

[60] Saghi, Z et al (2015) Reduced-dose and high-speed acquisition strategies for multi-dimensional electron microscopy. *Adv Struct Chem Imaging*, in-press.

Supplementary figures and movies

Supplementary figures

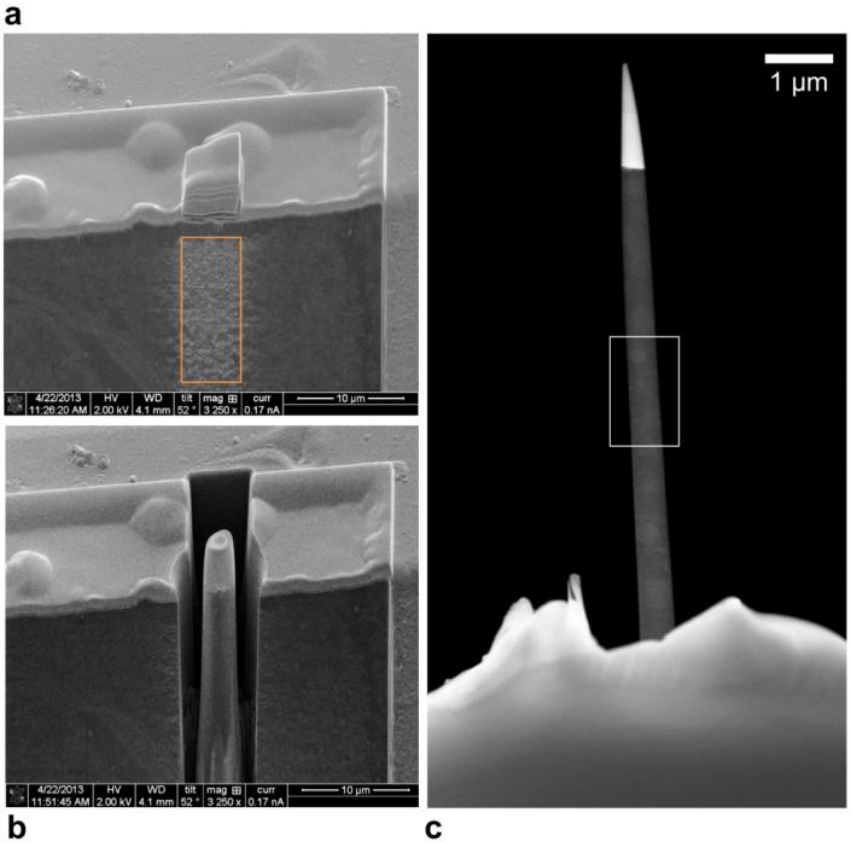

S1. FIB preparation of a needle-shaped sample for on-axis electron tomography. (a) The specimen is tilted towards the ion beam by 52˚, and a region of interest is selected (orange inset). A layer of platinum is deposited on the top surface in order to protect the selected region from implantation of Ga^+ ions. (b) A needle ca. 3 µm wide is produced by FIB milling over an annular area with an external diameter of 8 µm. An Omniprobe micro-manipulator is then used to remove the needle and weld it to a specimen cartridge compatible with the Fischione on-axis tomography holder. Further milling is carried out until a diameter of ca. 450 nm is reached. (c) ADF-STEM image of the produced needle, showing the volume selected for the tilt series acquisition (white inset).

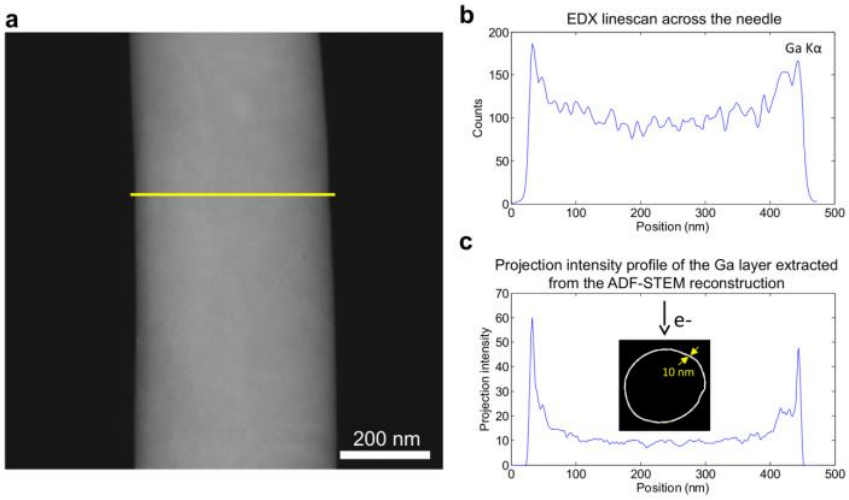

S2. Estimation of FIB-induced Ga+ implantation. (a) ADF-STEM image of the needle-shaped sample. (b) EDX linescan taken across the diameter of the needle (yellow line in (a)), showing a shell profile of the Ga Kα signal intensity with an average thickness of 10 nm. This is confirmed in (c) where the Ga layer is extracted from the ADF-STEM tomogram and used as test object to simulate the projection intensity profile of Ga Kα signal. The object is hollow to mimic EDX signal coming from Ga only. The asymmetric shape of the plots in (b) and (c) is due to the needle not being perfectly cylindrical. These measurements were performed using a TITAN Themis³ 300 TEM (FEI company) equipped with a Super-X EDX detector system (4 windowless silicon drift detectors). The EDX linescan was acquired at an acceleration voltage of 300 kV, in microprobe STEM mode, with a beam current of 1 nA and a dwell time of 1 second.

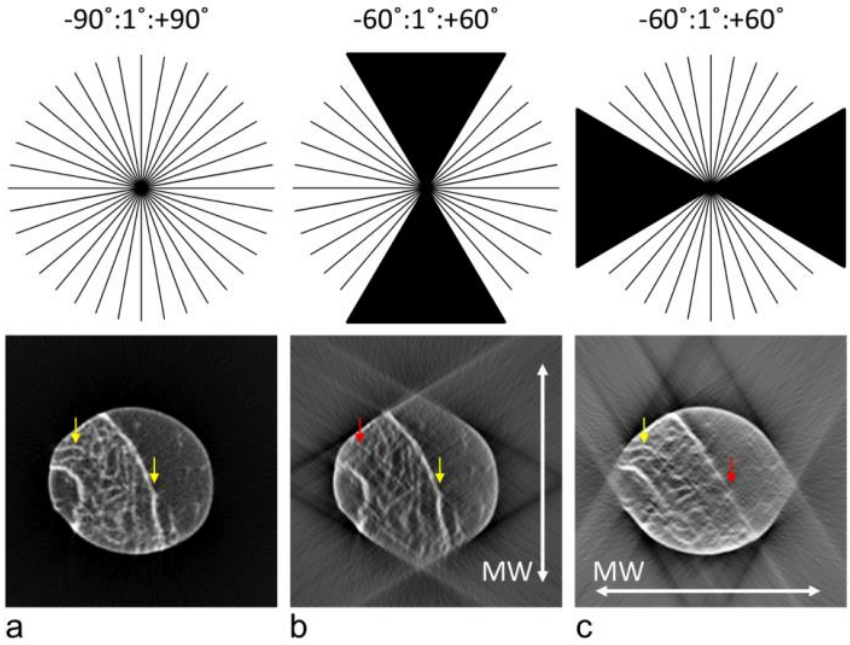

S3. Illustration of the relationship between the missing wedge direction and the orientation of features. (a) A fully sampled reconstruction retrieves both vertical and horizontal membranes (yellow arrows). (b) When the missing wedge is vertical (the unsampled region is shown in black in the Fourier space), vertical lines are retrieved (yellow arrow) but horizontal ones are lost (red arrow). (c) Reverse effect is observed when the missing wedge is horizontal. In an experimental setup, the missing wedge direction is fixed by the optic axis, and the scenarios in (b) and (c) correspond to different orientations of the sample in the *xz* plane (*z* being the optic axis).

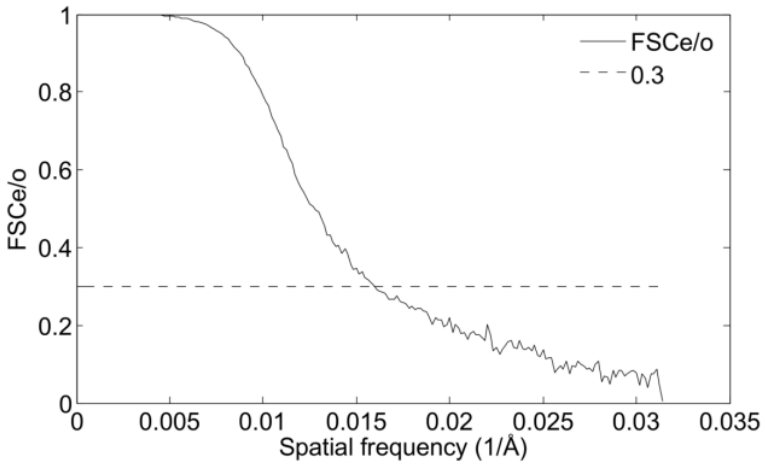

S4. Resolution estimation of the fully sampled reconstruction (tilt range: -90°:1°:+90°).

Subtomograms from even and odd members of the tilt series are produced by WBP in Inspect3D. A mask is applied to set the background (vacuum) to zero, and Bsoft is used to generate the even/odd FSC (FSCe/o) curve. The resolution, determined with a threshold of 0.3, is estimated to be 6.3 nm.

Supplementary movies

S5. Video of the full range tilt series.

S6. Video of the fully sampled WBP reconstruction.